

# Interfacial Interactions in Polypropylene–Organoclay–Elastomer Nanocomposites: Influence of Polar Modifications on the Location of the Clay

Zulima Martín,<sup>\*,†,⊥</sup> Ignacio Jiménez,<sup>‡</sup> Marian A. Gómez-Fatou,<sup>§</sup> Marcia West,<sup>||</sup> and Adam P. Hitchcock<sup>†</sup>

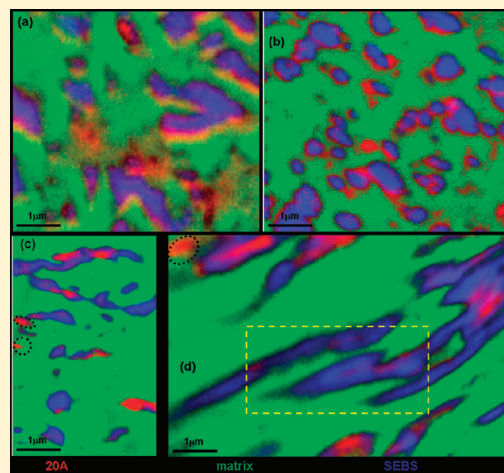
<sup>†</sup>Department of Chemistry and Brockhouse Institute for Materials Research, McMaster University, Hamilton, ON L8S 4M1 Canada

<sup>‡</sup>Instituto de Ciencia de Materiales de Madrid, ICMM-CSIC, Campus de Cantoblanco, 28049 Madrid, Spain

<sup>§</sup>Instituto de Ciencia y Tecnología de Polímeros, ICTP-CSIC, Juan de la Cierva 3, 28006 Madrid, Spain

<sup>||</sup>Health Sciences Electron Microscopy, McMaster University, Hamilton, ON L8S 4K1, Canada

**ABSTRACT:** A detailed, chemically sensitive study of the morphology of nanocomposites prepared by melt blending of polypropylene (PP) reinforced with an organically modified nanoclay (montmorillonite 20A) and toughened with poly(styrene-*b*-ethylenebutylene-*b*-styrene) (SEBS) is reported. Polar functionalities were incorporated in two ways: (i) additional compatibilizers: polypropylene-*graft*-maleic anhydride (PP-*g*-MA) and PP surface modified by N<sub>2</sub>-plasma treatment (PP\*) and (ii) superficial cold N<sub>2</sub> plasma modification of the elastomer SEBS (SEBS\*). In a previous study on the ternary composite PP/20A/SEBS [Martín et al. *Macromolecules* 2010, 43, 448] the montmorillonite 20A was found to be located inside the elastomer domains and not in direct contact with the PP phase. With the addition of polar functionalities, the nanoclay locates at the PP–SEBS interface rather than interacting just with the SEBS elastomer. Depending on the nature, content, and distribution of the polar groups in the material, the 20A locates selectively in the phase it has more affinity with. The different interactions between the polymer components and the nanoclay have been examined with X-ray diffraction (XRD), scanning electron microscopy (SEM), transmission electron microscopy (TEM), and scanning transmission X-ray microscopy (STXM). The latter provides simultaneously images with ~30 nm spatial resolution and quantitative compositional information at the same spatial resolution. Together this provides direct experimental evidence of the polar interactions in the composites. The influence of the nanoclay on the domain distributions of the elastomer is also discussed.



## INTRODUCTION

Addition of a nanophase reinforcing agent such as montmorillonite nanoclay to a polymer matrix leads to great improvements in properties such as thermal stability and mechanical performance at very low filler content.<sup>1–5</sup> The key factor for performance enhancement of polymer/clay nanocomposites is the dispersion of the high aspect ratio filler in the matrix since the final properties depend on the structure and morphology generated during the processing. Consequently, significant research effort is dedicated to characterizing the nanostructure of polymer nanocomposites.

In polypropylene (PP)-based nanocomposites an elastomer phase is normally used to compensate for the reduction of toughness caused by adding inorganic fillers.<sup>6,7</sup> The addition of styrene-*b*-ethylenebutylene-*b*-styrene triblock copolymer (SEBS) as a third component in the composite is intended to provide a better dispersion and intercalation of the nanoclay and also to provide a toughness improvement. In addition, it has been reported that in these kinds of blends of immiscible polymers, e.g.,

PS/PP<sup>8</sup> or PBT/PE,<sup>9</sup> the nanoclay acts by modifying the interphase properties and improves the compatibility between the different polymeric phases.

The right balance between stiffness and toughness provided by the incorporation of the filler and the elastomer, respectively, allows applications of these polymer nanocomposites as materials for automotive and structural materials in other industrial sections.<sup>10,11</sup> To achieve the desired mechanical properties, the nanoclay and elastomer particles must be finely and homogeneously dispersed in the polymer matrix.

In a previous study we examined the intercalation capability of SEBS in nanocomposites of isotactic PP with 5 wt % of organically modified montmorillonite (20A) prepared by melt blending.<sup>12</sup> We observed that the SEBS elastomer intercalated the 20A nanoclay and also encapsulated it. The 20A was always located inside the elastomer domains and not in direct contact

**Received:** November 28, 2010

**Revised:** January 21, 2011

**Published:** March 07, 2011

with the PP matrix, which is detrimental to the improvement in the mechanical properties of the matrix.<sup>11</sup> The reason that 20A interacts with SEBS rather than with PP was attributed to the higher polarity and surface energy of styrene in comparison with the polyolefinic components. It was found that the location of 20A and its degree of intercalation depended on the miscibility between the polymer and the organoclay.<sup>12–14</sup> To overcome the lack of polar affinity and to increase the nanoclay–matrix interactions, we explored two alternative compatibilization methods: (i) incorporation of additional compatibilizers: polypropylene-*graft*-maleic anhydride (PP-*g*-MA) a common polar compatibilizer and PP surface modified by N<sub>2</sub>-plasma treatment (labeled as PP\*) and (ii) superficial cold nitrogen plasma modification of the SEBS elastomer (labeled as SEBS\*). Unlike polymers with polar groups like polyamides,<sup>3,15–17</sup> in nonpolar polymers like PP the organic modification of the clay is not enough to achieve a good level of dispersion and barely leads to mixed structures.<sup>18–20</sup> Therefore, compatibilizers like PP-*g*-MA are commonly used to improve interactions between the organic polymers and the inorganic filler.<sup>21–24</sup> Cold plasma treatments have been also used for surface functionalization of polymers to improve the adhesion properties without affecting the characteristics of the bulk, by increasing the surface energies of the polymers through the generation of functional groups.<sup>25–28</sup> By surface modification with nitrogen cold plasma, a content of polar groups comparable with the functionalization in commercial compatibilizers is introduced in the PP and SEBS backbones.<sup>29</sup> The aim of this work is to investigate the structure, morphology, and interfaces of isotactic polypropylene–nanoclay–elastomer composites prepared by melt mixing with the aforementioned compatibilization strategies.

X-ray diffraction (XRD), scanning electron microscopy (SEM), and transmission electron microscopy (TEM) are often used to characterize the morphology and the intercalation capability of polymers. To date, most morphology characterization studies have used SEM, TEM, and/or atomic force microscopy (AFM).<sup>8,30–32</sup> However, these microscopies alone cannot provide conclusive information about the compatibilization role of the nanoclay or the SEBS in the PP–nanoclay–SEBS composites due to the lack of chemical contrast between the SEBS and PP polymeric phases. In principle, this could be overcome by staining one of the components, but this is quite difficult to perform selectively due to the similar chemical structure of both polymers. Besides, the large difference in the TEM magnifications needed to observe the rubber phase (in the range of micrometers) and the clays (in the range of nanometers) make it difficult to observe all three components simultaneously. In addition, compositional information with chemical speciation is not provided by electron microscopies, without electron energy loss spectroscopy (TEM-EELS), and core level TEM-EELS has significant limitations in application to polymeric materials like these due to radiation damage.

Here we investigate the morphology of these nanocomposites by scanning transmission X-ray microscopy (STXM). STXM is a very powerful tool for characterization of structured soft condensed matter nanomaterials<sup>33–35</sup> and has been part of our strategy to develop these materials.<sup>1,12</sup> Optimal characterization of such nanocomposites requires a microscopy technique with high spatial resolution and a spectroscopy technique with high chemical sensitivity. Contrast in STXM is based on differences in the near-edge X-ray absorption spectra (NEXAFS) of each component, which, as shown here, can readily differentiate all

components in these polypropylene–clay–elastomer nanocomposites. STXM provides quantitative chemical mapping at nanometer scales and hence both spatial and compositional chemical information are provided at the same time. The STXM results provide information on the interactions among the polymers and the nanoclay and the exact local morphology of the nanoclay with respect to the polymers. Since the properties of the composites depend on the size and on the distribution of the clay and the elastomer particles, particle analyses for both the filler and elastomer phases as determined by SEM, TEM, and STXM are also presented.

The purpose of this paper is to examine the effect on the morphology after modifying the polarity of the blend system by the addition of different kinds of polar groups. A change in the blend morphology with respect to the location of the 20A nanoclay at the interphase regions is expected. The first section of this paper evaluates the effect of incorporating polar groups by the addition of the PP-*g*-MA and PP\* (PP superficially modified with nitrogen cold plasma) compatibilizers. The second section evaluates the effect of the addition of SEBS elastomer superficially modified with nitrogen plasma (SEBS\*). As expected, the incorporation of polar functionalities leads to changes in the morphology of the nanocomposites which are related to changes in the location of the 20A nanoclay. The morphology characterization is addressed by SEM, XRD, and TEM while STXM spectromicroscopy provides key data about the location of the components and their interactions.

## EXPERIMENTAL SECTION

**Materials.** The polypropylene (PP) used as matrix was an isotactic homopolymer, provided by REPSOL, with a polydispersity of 4.77, an isotacticity of 95%, and a viscosity-average molecular weight of 179 000 g/mol.<sup>1,12</sup> The organically modified montmorillonite used was Cloisite 20A (20A) obtained from Southern Clay Products.<sup>1</sup> Its nominal formula is that of montmorillonite,  $M_y^+(Al_{2-y}Mg_y)Si_4O_{10}(OH)_2 \cdot nH_2O$ , where  $M^+$  is  $(CH_3)_2N^+(HT)$ , where HT is hydrogenated tallow, with a composition of (~65% C18; ~30% C16; ~5% C14) aliphatic hydrocarbons. The elastomer used was a triblock copolymer SEBS (Calprene H-6110) provided by DYNASOL, with 30 wt % of styrene content, a molecular weight value of  $M_w = 85\,000$  g/mol, and  $M_w/M_n = 1.45$ , as determined by gel permeation chromatography (GPC). The common compatibilizer used was polypropylene-*graft*-maleic anhydride (PP-*g*-MA) with a maleic anhydride content of 0.40 wt % and a viscosity-average molecular weight of 83 500 g/mol, EXXELOR PO1015 provided by EXXON.

**Cold Nitrogen Plasma Modification.** PP surface modified by N<sub>2</sub> plasma treatment, PP\*, was also used as a polar compatibilizer. Powder-like microparticles, from the same isotactic PP used for the matrix, were prepared and surface modified by N<sub>2</sub> cold plasma treatment. There was no significant reduction in the molecular weight (viscosity-average molecular weight is 172 000 g/mol). The prior processing of the PP, the plasma treatment conditions, and the characterization of the chemical nature, surface composition, and physical properties of PP\* have been reported previously.<sup>29</sup> The SEBS elastomer was modified under the same cold N<sub>2</sub> plasma treatment conditions to get SEBS\*. The content of polar groups in the plasma-modified species is on the order of 0.12%.<sup>29</sup>

**Preparation of Polypropylene–Montmorillonite (PP-20A) Composites.** Polymer composites were prepared by melt blending in a Haake Rheomix 600 internal mixer attached to a Haake Rheocord 90 corotating twin screw mixing chamber at 190 °C for 5 min at 100 rpm. SEBS loading was always 15 wt % and the 20A nanoclay (organic modified montmorillonite) loading was always 5 wt % as these have been

**Table 1. Statistical Analysis of SEM Photomicrographs: Size and Aspect Ratio of SEBS Domains<sup>a</sup>**

sample	av area SEBS domains <sub>SEM</sub> ( $\mu\text{m}^2$ ) <sup>b</sup>	SEBS domains $\langle\text{AR}\rangle_{\text{SEM}}$
PP/SEBS 90/10 <sup>c</sup>	1.30 ± 0.30	1.00 ± 0.15
PP/SEBS 80/20 <sup>c</sup>	1.30 ± 0.30	1.30 ± 0.50
PP/20A/SEBS 80/5/15 <sup>c</sup>	0.80 ± 0.35	1.90 ± 0.10
PP/20A/SEBS/PP-g-MA-5	0.60 ± 0.05	2.30 ± 0.30
PP/20A/SEBS/PP-g-MA-15	0.50 ± 0.05	1.50 ± 0.15
PP/20A/SEBS/PP*-5	0.75 ± 0.05	2.80 ± 0.60
PP/20A/SEBS/PP*-15	1.00 ± 0.10	2.20 ± 0.30

<sup>a</sup>The statistical analysis of particles shape and size was made from 100 particles of different slices of each sample. <sup>b</sup>Computed as the elliptical area of the cavities in the SEM images. <sup>c</sup>Data from previous studies.<sup>12</sup>

demonstrated to be the optimum content for mechanical performance.<sup>18,20,36</sup> In order to explore the influence of the polar group content, 5 and 15 wt % of PP-g-MA were incorporated to produce composites labeled PP/20A/SEBS/PP-g-MA-5 and PP/20A/SEBS/PP-g-MA-15, respectively. In order to compare the compatibilizer activity of PP\* with the commercial compatibilizer, the PP\* contents of 5 and 15 wt % were also used to produce composites labeled as PP/20A/SEBS/PP\*-5 and PP/20A/SEBS/PP\*-15. In the composite with SEBS treated with N<sub>2</sub>-plasma, SEBS\*, the content of the superficially modified elastomer was 15 wt % (labeled as PP/20A/SEBS\*). The interactions in this composite were also examined after the addition of 15 wt % of PP\* (labeled PP/20A/SEBS\*/PP\*-15). Tables 1 and 4 list all the materials examined. The equipment used for the superficial modification of the polymers was a homemade cold plasma apparatus described elsewhere.<sup>29</sup> Films of the nanocomposite material were compression-molded at 100 Mbar while heating the pellets at 190 °C for 5 min with subsequent quenching of the formed film between water-cooled metal plates.

**Characterization.** *XRD.* X-ray diffraction (XRD) was used to measure the interlayer spacing of the clay. XRD patterns were measured at room temperature using a Philips PW 1050/70 diffractometer, scanned at 1°/min in a 2 $\theta$  range between 2° and 35° using Ni-filtered Cu K $\alpha$  radiation. The level of intercalation in 20A is evaluated on the basis of the change of the nanoclay interlayer spacing from the 2 $\theta$  position of the (001) diffraction peak.

*SEM and TEM.* The composite morphology and the nanoclay dispersion were examined by scanning electron microscopy (SEM) and transmission electron microscopy (TEM). SEM images were obtained with a Philips XL30 ESEM, operating at an accelerating voltage of 25 kV. Samples were cryofractured from film specimens and the rubbery phase was extracted with heptane to observe the morphology of the cavities that correspond to the volume initially occupied by this phase. The fractured samples were coated with ~5 nm Au/Pd to avoid charging during electron irradiation. Transmission electron microscopy (TEM) images were obtained with a JEOL JEM 1200 EX TEMSCAN transmission electron microscope. Ultrathin sections, ~100 nm thick, were cryogenically microtomed with a diamond knife at ~-60 °C. Sections were collected on TEM grids.

*STXM.* Scanning transmission X-ray microscopy measurements were conducted at BL5.3.2.2 of the Advanced Light Source at Lawrence Berkeley National Laboratory.<sup>37,38</sup> The BL 5.3.2.2 STXM can provide images with ~30 nm spatial resolution for X-ray photons of 250–600 eV, with an energy resolution of about 0.1 eV. This energy range includes the most important absorption edges in polymer chemistry, C(1s) at 285 eV, N(1s) at 400 eV, and O(1s) at 530 eV. The near-edge X-ray absorption (NEXAFS) spectra of pure reference materials were scaled to the elemental linear X-ray absorption profile (thickness = 1 nm; densities (PP) = 0.9 g/cm<sup>3</sup>, (SEBS) = 1 g/cm<sup>3</sup>, and (20A) = 1.77 g/cm<sup>3</sup>) by

matching the recorded reference spectra to the elemental signal in the pre-edge (below 282 eV) and far continuum (above 320 eV). Sequences of images at photon energies encompassing the C(1s) and O(1s) regions were recorded to obtain chemical component maps. After alignment and conversion to optical density, the image sequences<sup>39</sup> were converted to chemical component maps using pixel-by-pixel singular value decomposition (SVD) curve fitting to the absolute-scale NEXAFS spectra of the pure components.<sup>1,12</sup> All data were analyzed using aXis2000.<sup>40</sup> The samples for the STXM experiments were prepared in the same fashion described above for the TEM measurements.

## RESULTS AND DISCUSSION

**PP/20A/SEBS/PP-g-MA and PP/20A/SEBS/PP\*.** *Electron Microscopy.* The typical SEBS phase-separated morphology in blends are shown in Figure 1, which compares SEM images of the fractured surfaces of the PP/20A/SEBS samples with the common compatibilizer PP-g-MA (micrographs a and a') and with PP\* as compatibilizer (micrographs b and b'). Micrographs a and b correspond to compatibilizer contents of 5 wt %, while micrographs a' and b' correspond to 15 wt % of compatibilizer. Previous SEM<sup>41</sup> and STXM<sup>12</sup> studies showed droplet dispersion morphology in PP/SEBS binary blends with a tendency to coalescence of SEBS domains when the elastomer content increased. In the ternary composite PP/20A/SEBS,<sup>12</sup> due to the presence of the nanoclay, SEBS domains became elliptical, presenting a reduction in the coalescence tendency and thus in the area of SEBS domains and a better distribution in the matrix (see Table 1). Note that the particle sizes values extracted from the SEM photomicrographs are relative since these might be affected by the morphology of the metal-coated fracture surface. In the case of the ternary composite PP/20A/SEBS, 20A was located inside the SEBS domains.<sup>12</sup> In the present samples, the addition of 5 wt % of the common compatibilizer PP-g-MA (Figure 1a) leads to no significant modification of the elastomer phase dispersion, but when the PP-g-MA content is increased to 15 wt % (Figure 1a'), there is a much better distribution of smaller SEBS domains. The aspect ratio (AR) has also decreased (Table 1). The shape of SEBS domains seems more spherical than elliptical. Interfacial activity of 20A localized at the interface could explain these changes in the SEBS domain sizes and distributions. It is known that the 20A exfoliation level in polymer nanocomposites increases when increasing the amount of polar groups.<sup>1</sup> This suggests that with 15 wt % of PP-g-MA the clay might be more exfoliated and have interactions with both matrix and elastomer phases. With the addition of the PP\* compatibilizer the SEBS domain shape stays elliptical (Figure 1b,b'). With 5 wt % of PP\* the elastomer domains are more elongated (higher AR), but with the same area as the ternary composite PP/20A/SEBS (Table 1). Increasing the PP\* content to 15 wt % seems to increase coalescence of the SEBS domains. The elastomer dispersion in the matrix is less homogeneous, and the area is remarkably bigger than the domain areas observed in the ternary composite PP/20A/SEBS and in the nanocomposites with the common compatibilizer PP-g-MA.

Figure 2 shows the XRD patterns of pristine 20A (*d* spacing (*d*<sub>001</sub>) of 2.52 ± 0.05 nm) and of the nanocomposites. The absence of the characteristic peak of 20A in the composites indicates exfoliation of the clay. In the case of the nanocomposite with 15 wt % PP\*, the diffraction peak of the clay is seen, but the peak intensity is significantly decreased and the interlayer spacing

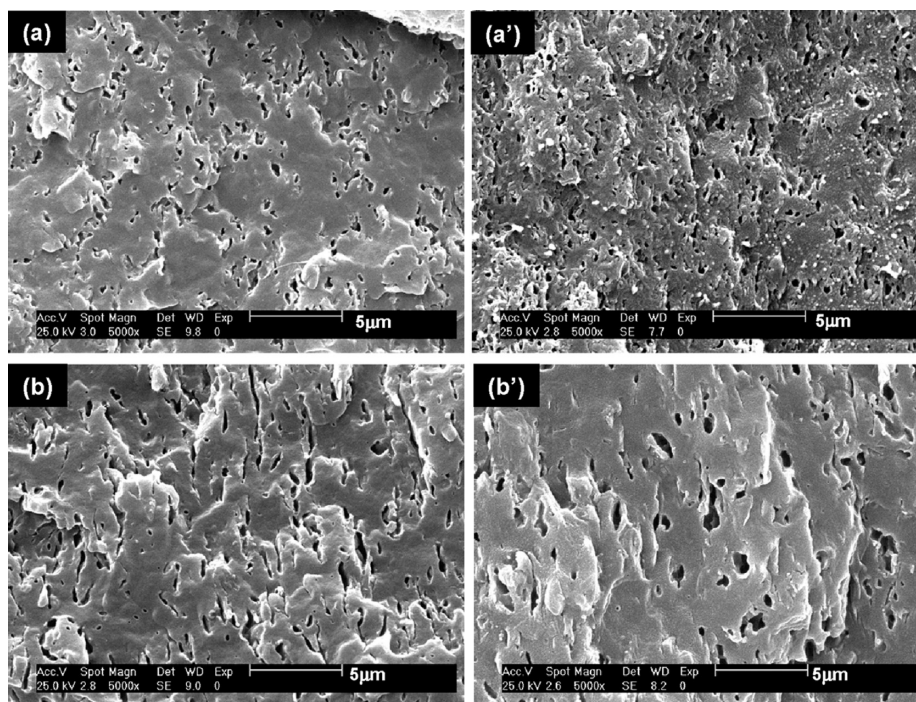


**Figure 1.** SEM images at 25 kV acceleration voltage of fracture surfaces of (a) PP/20A/SEBS/PP-g-MA-5, (a') PP/20A/SEBS/PP-g-MA-15, (b) PP/20A/SEBS/PP\*-5, and (b') PP/20A/SEBS/PP\*-15.

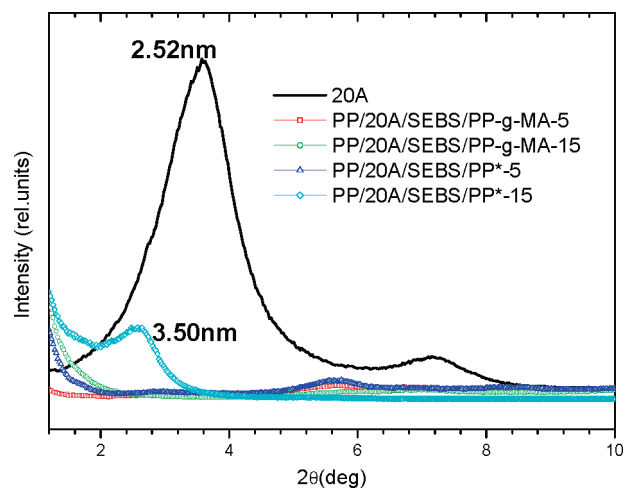


**Figure 2.** XRD patterns for pristine clay and for the nanocomposites. Insert number denotes the  $d_{001}$  of clay.

is increased to  $3.50 \pm 0.05$  nm, consistent with an intercalated structure.

SEM provides a large-scale overview of the SEBS domains dispersion in the matrix and XRD provides an average value for morphology of intercalated and exfoliated clays, but neither technique reveals how the 20A nanoclay interacts with the polymers. The clay dispersion and morphology of the nanocomposites was further characterized by TEM. Figure 3 shows TEM images at different magnifications of the nanocomposites. (a) and (a') correspond to PP/20A/SEBS/PP-g-MA-5, (b) and (b') to PP/20A/SEBS/PP-g-MA-15, (c) and (c') to PP/20A/SEBS/PP\*-5, and (d) and (d') to PP/20A/SEBS/PP\*-15. The statistical analysis of the size and morphology of the 20A is summarized in Table 2. With 5 wt % of PP-g-MA (Figure 3a,a'), even though

there is 20A still located within what appear to be SEBS domains, compared with the ternary composite without compatibilizer, PP/20A/SEBS,<sup>12</sup> here 20A inside of the SEBS domains is intercalated and tends to locate at the PP–SEBS interface as small stacks. Isolated layers are also observed in the matrix. When the common compatibilizer is increased to 15 wt %, 20A stacks are no longer visible (Figure 3b,b'). All of the 20A clay is finely exfoliated, and single layers are clearly visible, located mostly at the PP–SEBS interface. This confirms that the degree of exfoliation of the clay increases with increasing content of polar groups. Figure 3b shows there is an improvement in the SEBS domains dispersion when increasing the PP-g-MA content due to the higher exfoliation of the clay. With 5 wt % PP\* as compatibilizer (Figure 3c,c') 20A is observed to locate preferentially at the PP–SEBS interface rather than inside the elastomeric domains. Compared to the nanocomposites with 5 wt % of the PP-g-MA compatibilizer, with PP\* apparently there is no 20A inside of the SEBS domains, and the nanoclay appears as bigger stacks in which the clay platelets do not appear to line up, but rather are bent and twisted (see Figure 3c,c' and Table 2). The absence of the diffraction peak of 20A in this sample (Figure 2) is now explained by its complex morphology and the lack of order of the nanoclay, rather than by a complete exfoliation of the clay. However, when the PP\* content is increased to 15 wt % (Figure 3d,d') exfoliated single layers together with intercalated regions appear in a mixed morphology which also contains a few stacks, shorter and much thinner than with 5 wt % of PP\*.

**STXM X-ray Spectromicroscopy.** Despite the quality of the TEM photographs, the lack of chemical contrast makes it difficult to speak with certainty about the SEBS domains since there is no direct chemical identification. To gain further insight into the polymer–clay interactions in these samples, STXM spectroscopy was used to simultaneously observe and identify the components in the nanocomposites. Figure 4 shows the C(1s)

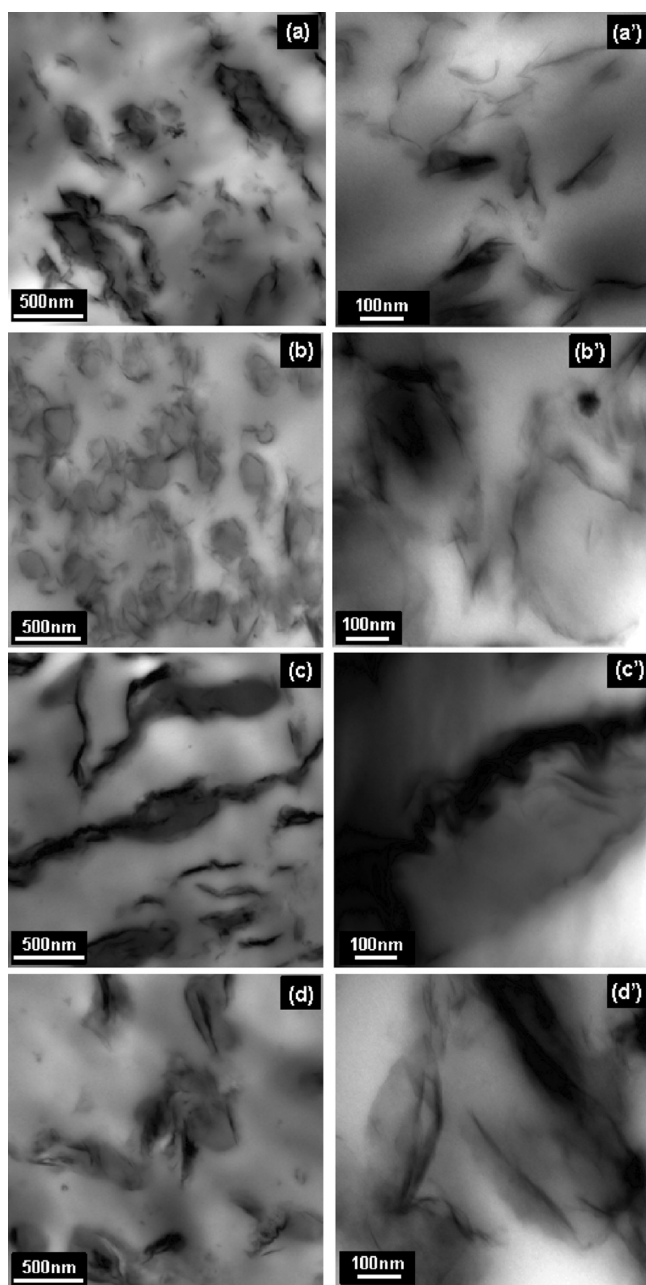


**Figure 3.** TEM images at different magnifications of the nanocomposites (a) and (a') PP/20A/SEBS/PP-g-MA-5, (b) and (b') PP/20A/SEBS/PP-g-MA-15, (c) and (c') PP/20A/SEBS/PP\*-5, and (d) and (d') PP/20A/SEBS/PP\*-15.

NEXAFS spectra of the components on an absolute intensity scale, after subtraction of a linear extrapolation of the pre-C(1s) signal. The lower three curves correspond to the matrix components, since compatibilizers and PP matrix are mixed homogeneously.<sup>1</sup> The spectra of the matrix components are dominated by the characteristic  $\sigma^*_{C-H}$  and  $\sigma^*_{C-C}$  peaks of polyolefins at 288 and 293 eV.<sup>42</sup> There are also very weak contributions from  $\pi^*_{C=C}$  states at 285 eV, corresponding to minor compatibilizer contributions. In the case of PP-g-MA, the 285 eV signal is due to double bonds from the maleic group, and in the case of PP\*, it is due to the slight surface cross-linking produced by the plasma treatment.<sup>29</sup> In general, the C(1s) spectra from the three polyolefins

are similar, indicating that the content of polar groups in the compatibilizers is not enough to provide a noticeable signal at the carbon absorption edge.

The C(1s) spectra of the elastomers (SEBS, SEBS\*) (middle curves) and the organoclay (20A) (upper curve) all have strong signals at 285 eV. In the case of the elastomers this is due to the  $\pi^*_{C=C}$  state of the styrene group. The C 1s signal in 20A is much weaker than in the other species (see vertical scales of Figure 4), consistent with the low organic loading. The 20A spectrum contains a 285 eV peak indicating the presence of C=C bonds, which is at slightly lower energy and broader than the corresponding  $\pi^*_{C=C}$  peak in SEBS. There is also a broad peak at 289.5 eV in the  $\sigma^*_{C=O}$  region, corresponding to partial oxidation of the organic components giving rise to this C(1s) spectrum.

The chemical composition maps derived from STXM image sequences measured from 278 to 320 eV are shown in Figure 5 for the nanocomposites PP/20A/SEBS/PP-g-MA-5 (Figure 5a), PP/20A/SEBS/PP-g-MA-15 (Figure 5b), PP/20A/SEBS/PP\*-5 (Figure 5c), and PP/20A/SEBS/PP\*-15 (Figure 5d). The colors represent different chemical components in the nanocomposites. Red regions correspond to the 20A nanoclay, green regions to PP matrix, and blue to SEBS. Intermediate colors indicate the presence of several components in one pixel. The first observation from the STXM maps is that the phase separation of SEBS and PP components remains in all cases. In PP/20A/SEBS/PP-g-MA-5 (Figure 5a) it is evident that the clay particles locate preferentially at the matrix–elastomer interface. The purple pixels, corresponding to mixing of 20A (red) and SEBS (blue), and the yellow-orange pixels, corresponding to mixing of 20A (red) and the matrix (green), indicate that the clay particles are fully intercalated by SEBS and by the compatibilizer, respectively, at the matrix–elastomer interface. The nanoclay 20A is associated with the SEBS domains. However, it is not encapsulated inside of the elastomeric phase, like in the ternary nanocomposites PP/20A/SEBS,<sup>12</sup> but rather located at the boundaries between the SEBS domains and the PP matrix. Some small and isolated clay stacks are also found in the matrix. With increased compatibilizer, in PP/20A/SEBS/PP-g-MA-15 (Figure 5b), there is an even more dramatic change in morphology. There is a significant reduction in the size of the elastomeric domains and a change in their shape, now spherical, which is clear evidence of improved dispersion of the clay. The exfoliated layers interact with both polymer phases, as is evident in the imaged structure. The clay platelets act as an interfacial compatibilizer and lead to a reduction in interfacial tension which inhibits coalescence of the SEBS domains and therefore reduces the size of the SEBS domains. What could be intuited by SEM, XRD, or TEM, it is now confirmed by STXM. The finely exfoliated nanoclay locates preferentially at the matrix–SEBS interface. There is also 20A dispersed within the matrix, as evidenced by the red-orange pixels present in the matrix with no contact with the SEBS domains. No clay is visible inside of the elastomeric domains. It is known that the 20A nanoclay increases the melt viscosity affecting the dispersion of the elastomer phase and slowing down the tendency of the elastomer to coalescence.<sup>12</sup> In PP/20A/SEBS/PP-g-MA-15 (Figure 5b), the larger number of polar groups in the matrix leads to greater exfoliation of the nanoclay, a better distribution of it in both PP-SEBS interface and matrix, reducing the interfacial tension, which contributes further to reduction of the elastomer coalescence. SEBS domains have a homogeneous size and they are homogeneously distributed in the matrix. Table 3 summarizes the elastomer particle size analyses from

**Table 2. Statistical Analysis of TEM Photomicrographs: Size and Aspect Ratio of 20A Clay Particles<sup>a</sup>**

sample	isolated layers average length <sub>TEM</sub> (nm)	20A stacks (AR) <sub>TEM</sub>
PP/20A/SEBS 80/5/15 <sup>b</sup>	320 ± 70	8 ± 1
PP/20A/SEBS/PP-g-MA-5	200 ± 30	8.0 ± 0.5
PP/20A/SEBS/PP-g-MA-15	160 ± 10	<i>c</i>
PP/20A/SEBS/PP*-5	310 ± 80	18 ± 3
PP/20A/SEBS/PP*-15	250 ± 20	27 ± 2

<sup>a</sup>The statistical analysis of particles shape and size was made from 30 particles of different slices of each sample. <sup>b</sup>Data from previous studies. <sup>12</sup>

<sup>c</sup>No stacks.

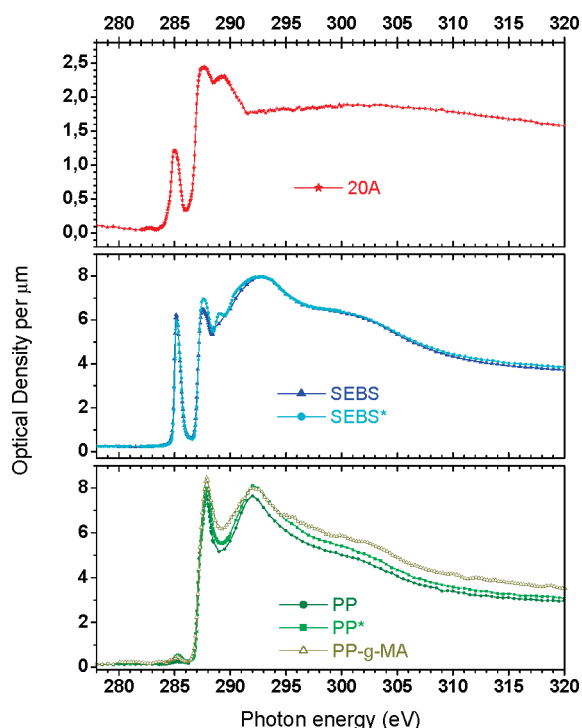


**Figure 4.** (a) NEXAFS spectra at the C(1s) edge of the pristine components: PP (olive squares), PP\* (green circles), PP-g-MA (dark yellow triangles), 20A (red stars), SEBS (blue triangles), and SEBS\* (cyan circles). The spectra are plotted on an absolute linear absorbance scale after subtracting a linear background extrapolated from the pre-C(1s) signal.

STXM images. The aspect ratio of the SEBS domains is close to 1, and the average area is much smaller than the average area of SEBS observed in the other composites studied in this work. With STXM, the SEBS domains are directly observed without any artifact; thus, Table 3 shows true size values. The cavities in the heptane-extracted composites measured by SEM (Table 1) have larger average areas than in the direct measurements by STXM, although the aspect ratios are similar.

Figure 5c shows the chemical compositional map for PP/20A/SEBS/PP\*-5, the nanocomposite containing 5 wt % of PP\*. The SEBS domains appear with heterogeneous sizes, but most of them have a very elongated shape, with an average aspect ratio of  $3.0 \pm 1.2$ . The most significant difference compared to the common compatibilizer PP-g-MA is that, even though there is a slight tendency of the nanoclay to locate at the rim of the SEBS

domains, the 20A is not located at the PP–SEBS interface, but rather it is located inside the elastomeric domains, despite what the TEM images (Figure 3c,c') indicate. Figure 5c does explain the twisted structure observed in Figure 3c'. Inside of the SEBS domains, the nanoclay twist during the intercalation process due to obstacle that SEBS encapsulation poses,<sup>12</sup> which prevents the 20A layers from dispersing in the PP matrix.<sup>12</sup> When the content of polar groups is increased to 15 wt % of PP\* (Figure 5d), there is an evident change in the shape and distribution of the SEBS domains. 20A is not found at the PP–SEBS interfaces or within the matrix, but inside of the elastomeric domains. The most remarkable observation is the large increase in coalescence of the SEBS domains. The elastomeric domains have an average area of  $1.1 \pm 0.3 \mu\text{m}^2$ , which is even bigger than the average area of the SEBS domains for the ternary composite PP/20A/SEBS (Table 3). Another detail that attracts attention is that the SEBS domain boundaries in this sample are not sharp, but rather it looks like the SEBS is merging into the matrix.

The nanocomposites with PP\* present a faint improvement on the ternary composite PP/20A/SEBS. The SEBS domains are better distributed, the nanoclay presents a slight tendency to locate toward the domain edges, and some small nanoclay stacks are observed in the matrix (marked in Figure 5c,d with dotted circles). These observations indicate that there are polar interactions between PP\* and 20A. However, the distributions of the 20A and SEBS domains are far from optimum, 20A does not seem to interact directly with the matrix, and it appears like there are stacks with a big aspect ratio (Table 2); therefore, the SEBS domains are significantly deformed, since they are wetting the clay stacks, adopting their shape. Clearly, the polar interactions among the components are very different between PP-g-MA and PP\*.

The polar groups in the common compatibilizer PP-g-MA, homogeneously mixed with the PP matrix, interact with the 20A rather than with SEBS. The affinity between PP-g-MA and 20A is stronger than that between 20A and SEBS and the nanoclay locates at the PP-SEBS interface and not inside the SEBS domains. Also, when the amount of PP-g-MA compatibilizer is increased, the degree of exfoliation of the clay increases. In the case of the PP\* compatibilizer, the polar groups do not seem to have a preferential affinity with the nanoclay, but they do interact with both 20A and SEBS. The interactions between PP\* and 20A explain the slight improvement in the clay location and the better distribution of the SEBS domains than in the ternary nanocomposite PP/20A/SEBS.<sup>12</sup> The interactions between PP\* and SEBS may explain why the SEBS domains are not sharp. There is another factor that may be related to differences between the two compatibilizers. Plasma treatment produces a slight superficial cross-linking in the polypropylene backbone chains which causes small differences between the crystallization process of the pristine PP (matrix) and the PP\*.<sup>29</sup> Even though PP and PP\* are completely compatible, in a quaternary blend, like PP/20A/SEBS/PP\* the PP\* polar groups interact with the components with which they have more affinity, which are 20A and the polystyrene groups of SEBS in this case. This might cause the PP\* in the matrix to collocate with the SEBS and 20A during the crystallization of the sample. The cross-linked chains of PP\* could have an enclosing effect hindering the 20A dispersion and facilitating the coalescence of the SEBS domains.

Figure 6a shows the STXM image at 285.2 eV of a portion of the region of PP/20A/SEBS/PP\*-15 indicated by dotted rectangle in Figure 5d, which contains a typical clay, SEBS, PP\*, PP interface. Figure 6b shows the same region of the color composite map.

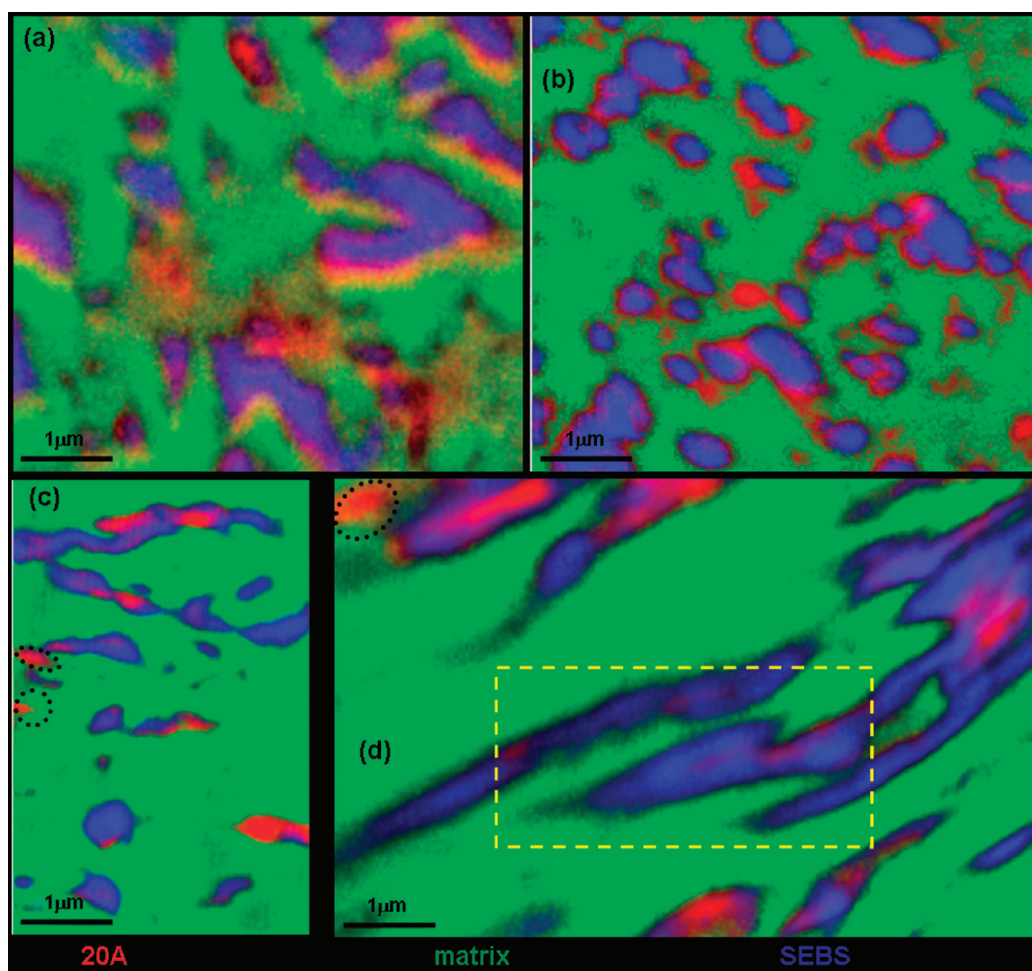


**Figure 5.** STXM composition maps of (a) PP/20A/SEBS/PP-g-MA-5 ( $6\ \mu\text{m} \times 5\ \mu\text{m}$ ), (b) PP/20A/SEBS/PP-g-MA-15 ( $6\ \mu\text{m} \times 5\ \mu\text{m}$ ), (c) PP/20A/SEBS/PP\*-5 ( $3.5\ \mu\text{m} \times 5\ \mu\text{m}$ ), and (d) PP/20A/SEBS/PP\*-15 ( $8\ \mu\text{m} \times 5\ \mu\text{m}$ ). The dotted circles mark nanoclay stacks. The dotted rectangle in (d) refers to Figure 6. STXM maps are derived from C(1s) image sequences recorded from 272 to 320 eV. The intensity scale of each color is rescaled to span the full range of each component.

**Table 3. Statistical Analysis of STXM Images: Size and Aspect Ratio of SEBS Domains<sup>a</sup>**

sample	av area SEBS domains <sub>STXM</sub> ( $\mu\text{m}^2$ ) <sup>b</sup>	SEBS domains $\langle\text{AR}\rangle_{\text{STXM}}$
PP/SEBS 90/10 <sup>c</sup>	$0.6 \pm 0.1$	$1.00 \pm 0.05$
PP/SEBS 80/2 <sup>c</sup>	$0.8 \pm 0.1$	$1.3 \pm 0.1$
PP/20A/SEBS 80/5/15 <sup>c</sup>	$0.30 \pm 0.05$	$1.8 \pm 0.2$
PP/20A/SEBS/PP-g-MA-5	$0.40 \pm 0.05$	$2.10 \pm 0.15$
PP/20A/SEBS/PP-g-MA-15	$0.15 \pm 0.05$	$1.35 \pm 0.05$
PP/20A/SEBS/PP*-5	$0.35 \pm 0.15$	$3.0 \pm 1.2$
PP/20A/SEBS/PP*-15	$1.1 \pm 0.3$	$2.4 \pm 0.5$

<sup>a</sup> The statistical analysis of particles shape and size was made from 100 particles of different slices of each sample. <sup>b</sup> Computed as the elliptical area of the SEBS domains observed in the STXM images. <sup>c</sup> Data from previous studies.<sup>12</sup>

C(1s) NEXAFS spectra, which were extracted along the yellow rectangle outlining the PP/SEBS boundary at the locations of the colored rectangles in Figure 6b, are plotted in Figure 6c. There is a very systematic change from a SEBS-like to a PP-like spectrum across the interface. The styrene group in SEBS leads to a very

sharp, intense  $\pi^*(\text{C}=\text{C})$  peak at 285.2 eV, but the 285.2 eV peak in the red spectrum, which is from the edge and some of the interior of the SEBS domain, is much less intense. This indicates that both PP\* and SEBS are present in the selected area, thereby confirming the PP\* is allowing interaction between the PP and SEBS components even though they are 100% immiscible in the absence of a compatibilizer.

To further verify the polar interactions between PP\* and 20A, we used STXM measurements at the O(1s) edge (520–570 eV). Figure 7a shows the O(1s) NEXAFS spectra of 20A, PP\*, and PP. The scaling factors to obtain the same height are indicated in the figure. The O(1s) absorption signal in PP is very low (the PP spectrum in Figure 7a has been scaled by a factor of 190), as PP does not intrinsically contain any oxygen. The O(1s) NEXAFS spectrum of PP is assigned to environmental contamination in the form of adsorbed water due to the hygroscopic character of PP plus a small amount of oxidized hydrocarbon. The oxygen content of PP\* is much larger ( $\times 30$ ) than that of PP. Its O(1s) spectrum is similar to that of PP, but the spectral features are more distinct. The spectrum is attributed to oxidation of surface free radicals created by the plasma when the sample is exposed to ambient atmosphere or by surface radicals interacting with residual oxygen in the treatment gas.<sup>29</sup> PP\* shows a well-defined

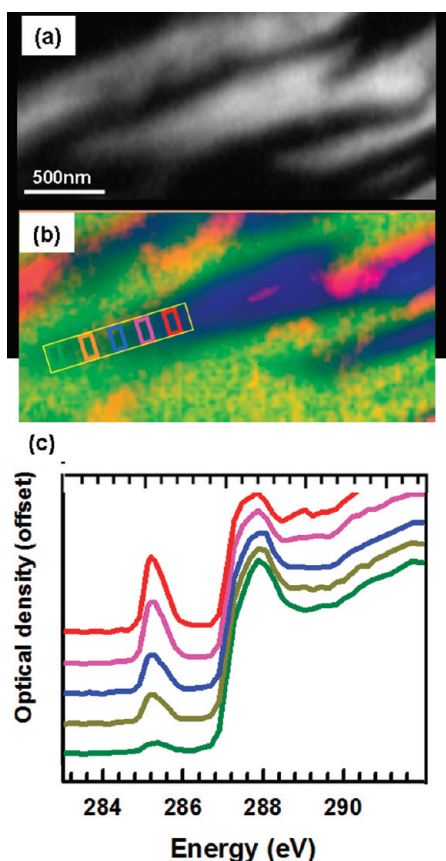


**Figure 6.** (a) STXM image at 285.2 eV of the area outlined in Figure 5d, which contains a typical clay, SEBS, PP\*, PP interface. Lighter regions indicate stronger X-ray absorption. (b) Same region of the color composite map mapped in Figure 5d. (c) C(1s) NEXAFS spectra at selected locations indicated by colored rectangles across the interface.

$\pi^*_{C=O}$  peak at 531.5 eV and a broad  $\sigma^*_{C-O}$  peak at 539 eV. The O(1s) spectrum of 20A is the most intense. It is dominated by the  $\sigma^*(Si-O)$  signal of the silicate. Figure 7b shows the color-coded chemical composition map from the PP/20A/SEBS/PP\*-15 sample derived from the O(1s) STXM image sequence (red corresponds to 20A, green corresponds to PP, and blue corresponds to PP\*). Because of the small oxygen signal of the PP, the component map for the PP has a very low S/N ratio. This results in the appearance of the green signal as a background. Purple pixels, which correspond to mixing of 20A (red) and PP\* (blue), are observed, confirming the polar interaction between PP\* and the clay. Although the PP matrix and PP\* are mixed without apparent phase separation, there is a clear dominance of PP\* in the vicinity of the 20A, and the great majority of nanoclay particles appear completely in purple, which correspond to clay particles fully intercalated by the PP\* compatibilizer.

**PP/20A/SEBS\* and PP/20A/SEBS\*/PP\*-15.** Figure 8 shows SEM images of the fracture surfaces of the PP/20A/SEBS\* (Figure 8a) and PP/20A/SEBS\*/PP\*-15 (Figure 8b) nanocomposites prepared with the SEBS elastomer superficially modified with cold nitrogen plasma, SEBS\*. In the PP/20A/SEBS\* sample (Figure 8a), the SEBS\* domains are quasi-spherical particles with an aspect ratio of  $1.35 \pm 0.30$  and a relatively large average area,  $0.90 \pm 0.02 \mu\text{m}^2$  (Table 4). It is generally recognized that for

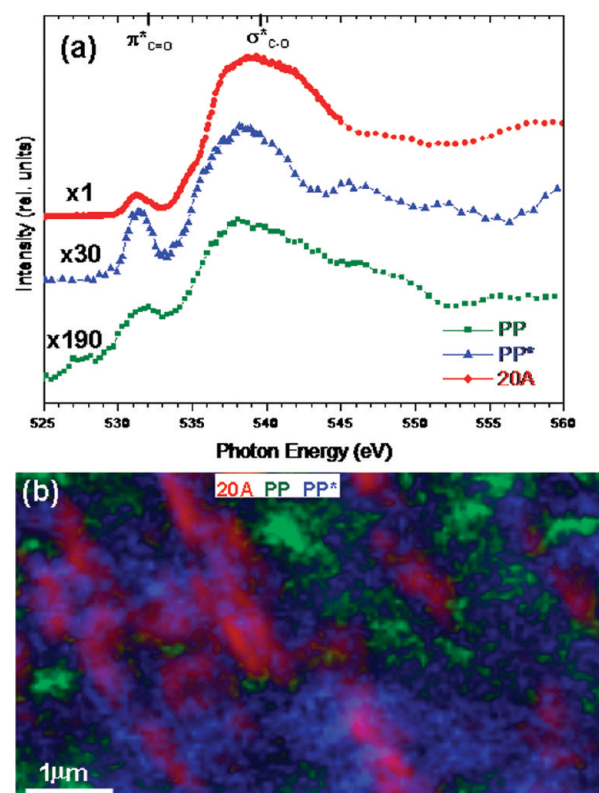


**Figure 7.** (a) NEXAFS spectra at the O(1s) edge of montmorillonite 20A (red circles), PP\* (blue triangles), and PP matrix (green squares). A linear background has been subtracted, and the inverse of the scale factors indicates the relative intensity of the O(1s) signals. (b) STXM composition maps of PP/20A/SEBS/PP\*-15 ( $6 \mu\text{m} \times 4 \mu\text{m}$ ) recorded from 510 up to 570 eV.

small size dispersed particles in blends elongated shapes are typically not formed due to interfacial tension considerations.<sup>43</sup> In this case, the size of the particles is much bigger than other elongated particles observed in this study (see Tables 1 and 4). In the PP/20A/SEBS\*/PP\*-15 sample (Figure 8b) the SEBS\* domains become elongated, aspect ratio of  $2.5 \pm 0.8$  (Table 4). The presence of polar groups in the matrix modifies the SEBS\* phase.

The XRD patterns of these nanocomposites (Figure 9) are completely devoid of the characteristic peak of 20A, indicating that the structure is intercalated or exfoliated to a very high degree, due to the presence of the polar groups. TEM micrographs of the PP/20A/SEBS\* sample (Figure 10a,a') show that most of the clay appears as small stacks both close to what are most likely SEBS\* domains as well as dispersed in the matrix. In the higher resolution image (Figure 10a'), exfoliated and intercalated layers are observed. After adding PP\* (Figure 10b) the clay platelets appear as stacks dispersed in the matrix in the form of long and thin curved bundles. The nanoclay is located preferentially at the boundaries of what might be a SEBS\* domain (Figure 10b'). Exfoliated layers are visible in the matrix as well as inside of the SEBS\*. The statistical analysis of the size and morphology of the 20A is summarized in Table 4. In general, the 20A distribution in the sample with SEBS\* is similar to that observed for the PP/20A/SEBS/PP-g-MA-5 sample while the 20A distribution for the PP/20A/SEBS\*/PP\*-15 sample is similar to that observed in PP/20A/SEBS/PP\*-5 and -15.

Figure 11 shows the color-coded composite of chemical component maps derived from a C(1s) STXM image sequence

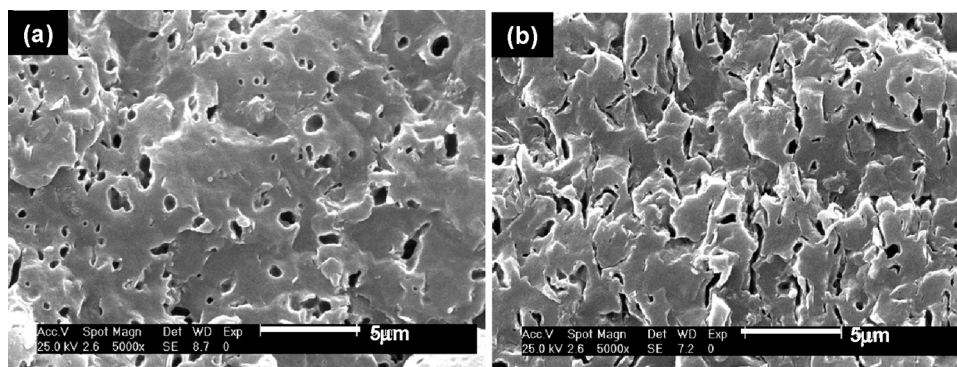


Figure 8. SEM images at 25 kV acceleration voltage of the fracture surface of (a) PP/20A/SEBS\* and (b) PP/20A/SEBS/PP\*-15.

Table 4. Elastomer and Clay Particle Size Analysis for the Nanocomposites Containing SEBS\*

sample	av area SEBS domains <sub>SEM</sub> ( $\mu\text{m}^2$ ) <sup>a</sup>	SEBS domains $\langle\text{AR}\rangle_{\text{SEM}}$	isolated 20A layers av length <sub>TEM</sub> (nm)	20A stacks $\langle\text{AR}\rangle_{\text{TEM}}$	av area SEBS domains <sub>STXM</sub> ( $\mu\text{m}^2$ ) <sup>b</sup>	SEBS domains $\langle\text{AR}\rangle_{\text{STXM}}$
PP/20A/SEBS*80/5/15	$0.90 \pm 0.02$	$1.3 \pm 0.3$	$350 \pm 100$	$10 \pm 1$	$0.70 \pm 0.03$	$1.2 \pm 0.2$
PP/20A/SEBS*/PP*-15	$0.70 \pm 0.03$	$2.5 \pm 0.8$	$230 \pm 25$	$9 \pm 4$	$0.45 \pm 0.10$	$1.9 \pm 0.4$

<sup>a</sup> Computed as the elliptical area of the cavities in the SEM images. <sup>b</sup> Computed as the elliptical area of the SEBS domains observed in the STXM images.

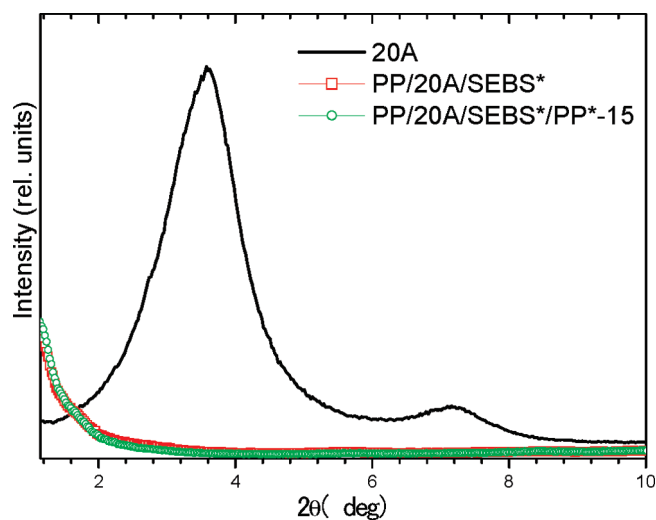


Figure 9. XRD patterns for pristine clay (black line) and for the nanocomposites: PP/20A/SEBS\* (red squares) and PP/20A/SEBS\*/PP\*-15 (green circles). Insert number denotes the  $d_{001}$  of clay.

(278–320 eV) for the PP/20A/SEBS\* (Figure 11a) and PP/20A/SEBS\*/PP\*-15 (Figure 11b) nanocomposites. Red is 20A, green is the matrix, and blue is SEBS\*. In PP/20A/SEBS\* (Figure 11a) there is a clear affinity between 20A and SEBS\*. 20A is barely visible inside of the elastomeric but is clearly visible as small stacks at the PP–SEBS\* interface. The surface plasma treatment of SEBS is efficient, and the nanoclay has more affinity for the polar groups at the SEBS\* surface than for the PS groups of the elastomer; thus, the clay prefers to locate at the PP–SEBS\* interface rather than inside the elastomeric domains. However, the intercalation/exfoliation level of the 20A nanoclay is low, as there is relatively few purple pixels, which would indicate 20A (red) intercalated by SEBS\* (blue). Because of the higher surface energy of SEBS\* and the absence of polar groups in the matrix, 20A is not dispersed in the matrix but rather surrounds the SEBS\*

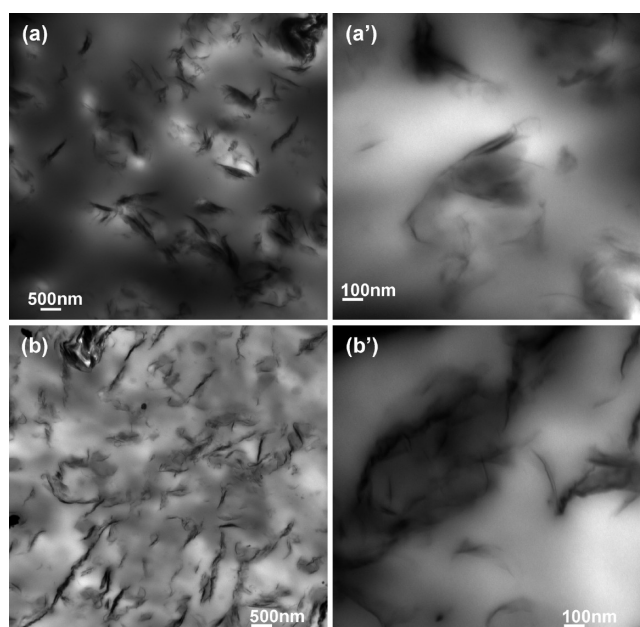
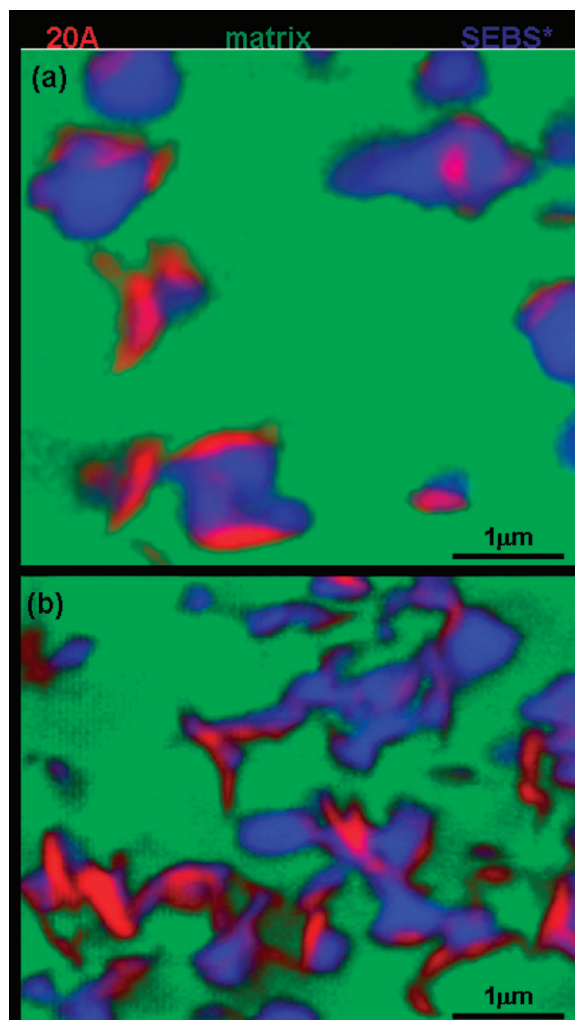


Figure 10. TEM images at different magnifications of the nanocomposites (a) and (a') PP/20A/SEBS\* and (b) and (b') PP/20A/SEBS\*/PP\*-15.

domains mostly as small stacks. Since 20A is not inside the elastomer domains, these have a spherical shape. The poor dispersion of the clay also explains the bigger average area of the SEBS\* domains. Only when the 20A is finely exfoliated in the matrix and/or at the PP–SEBS interface does the interfacial tension between PP and SEBS become reduced, so that the coalescence tendency of SEBS domains and consequently domains size decrease, as in PP/20A/SEBS/PP-g-MA-15 composite (Figure 5b).

In PP/20A/SEBS\*/PP\*-15 (Figure 11b), the addition of PP\* produces a dramatic change in the morphology. The size, shape, and distribution of the SEBS\* domains and the 20A nanoclay change (Table 4). Apparently, PP\* interacts with both SEBS\* and 20A.



**Figure 11.** STXM composition maps recorded from 272 up to 320 eV of (a) PP/20A/SEBS\* ( $5\ \mu\text{m} \times 5\ \mu\text{m}$ ) and (b) PP/20A/SEBS\*/PP\*-15 ( $5\ \mu\text{m} \times 4\ \mu\text{m}$ ). The color intensities are relative to each component.

Unlike in PP/20A/SEBS/PP\*-5 and -15 (Figure 5c,d), where the nanoclay preferentially locates inside the SEBS domains, in PP/20A/SEBS\*/PP\*-15 the balance of interactions among 20A, SEBS\*, and PP\* is different. Even though there is some 20A inside the SEBS\* domains, the clay shows a strong tendency to locate at the interface because of the interaction between 20A and SEBS\*. Overall, this nanocomposite presents a mixed structure. The nanoclay inside of the elastomeric domains appears as purple pixels, indicating that it is intercalated/exfoliated. When it is located at the PP–SEBS\* interface, the nanoclay is in the form of small stacks of platelets. Regarding to SEBS\* domains, these have a heterogeneous distribution. When 20A is located inside of the elastomeric domains due to its preferential interaction with PP\* and the associated enclosing effect, the SEBS\* domains adopt the shape of the 20A stacks such that they appear elongated with an irregular shape. When 20A is located at the PP–SEBS\* interface due to its preferential interaction with SEBS\*, the elastomeric domains keep a spherical shape.

## CONCLUSIONS

The effect of a combination of organomodified clay (montmorillonite 20A) and several different compatibilizers on the

morphology of PP/SEBS blends was investigated by several techniques including SEM, XRD, TEM, and STXM. The study showed that 20A can be selectively located in one or another of the polymers phases, depending on the ability of the compatibilizers to react with the components. Compared with the PP/20A/SEBS ternary nanocomposite, all the compatibilizers studied showed some level of improvement in the dispersion of the clay and SEBS domains. The compatibilization process was more efficient when PP-g-MA was incorporated since that ensures the presence of polar groups with a clear preferential affinity for the clay homogeneously dispersed in the PP matrix. With the addition of 5 wt % of PP-g-MA, 20A showed a tendency to locate at the PP–SEBS interface. The increase of the content of polar groups up to 15 wt % of PP-g-MA resulted in a fine exfoliation of the clay located at the PP–SEBS interface and in the matrix, and consequently, in dramatic decrease in interfacial tensions and thus in the SEBS domains size. When PP\* was used as compatibilizer, there was little improvement even though PP\* intercalated the clay. Because of the affinity of PP\* for both clay and SEBS domains an enclosing effect on the clay and SEBS domains was observed, hindering suitable dispersion of the clay and contributing to a tendency for elastomer coalescence. In the PP/20A/SEBS\* sample, 20A had a dramatic affinity for SEBS\* at the PP–SEBS\* interface, but the lack of polar groups in the matrix produced a concentration of 20A stacks around the SEBS domains. When PP\* was incorporated into this composite, the balance of interactions between SEBS\*/20A and PP\* with both 20A and SEBS\* led to localization of the clay both at the interface and inside SEBS\* domains, even though intercalated/exfoliated clay was not observed in the matrix.

## AUTHOR INFORMATION

### Corresponding Author

\*E-mail: zmartin@lbl.gov.

### Present Addresses

<sup>†</sup>Lawrence Berkeley National Laboratory, Berkeley, CA.

## ACKNOWLEDGMENT

We thank David Kilcoyne and Tolek Tyliczszak for expert maintenance of STXM 5.3.2.2 at the ALS. The ALS is supported by the Director of the Office of Science, Department of Energy, under Contract No. DE-AC02-05CH11231. Plasma modification of the polymers was financed by MICINN project MOS-PLADER MAT2009-13625.

## REFERENCES

- (1) Martin, Z.; Jiménez, I.; Gómez, M. A.; Ade, H.; Kilcoyne, A. L. D.; Hernández-Cruz, D. *J. Phys. Chem. B* **2009**, *113*, 11160–11165.
- (2) Vaia, R. A.; Jandt, K. D.; Kramer, E. J.; Giannelis, E. P. *Macromolecules* **1995**, *28*, 8080–8085.
- (3) Ray, S. S.; Okamoto, M. *Prog. Polym. Sci.* **2003**, *28*, 1539–1641.
- (4) Thostenson, E. T.; Chou, C.L.T.-W. *Compos. Sci. Technol.* **2005**, *65*, 491–516.
- (5) Kalaitzidou, K.; Fukushima, H.; Miyagawa, H. *Polym. Eng. Sci.* **2007**, *47*, 1796–1803.
- (6) Premphet-Sirisinha, K.; Preechachon, I. *J. Appl. Polym. Sci.* **2003**, *89*, 3557–3562.
- (7) Liang, J. Z. *J. Appl. Polym. Sci.* **2000**, *77*, 409–417.
- (8) Ray, S. S.; Pouliot, S.; Bousmina, M.; Utracki, L. A. *Polymer* **2004**, *45*, 8403–8413.

- (9) Hong, S. H.; Namkung, H.; Ahn, K. H.; Lee, S. J.; Kim, C. *Polymer* **2006**, *47*, 3967–3975.
- (10) Edward, P. M. *Polypropylene*; Hanser Publishers: Munich, 1996.
- (11) Bao, S. P.; Tjong, S. C. *Composites A* **2007**, *38*, 378–387.
- (12) Martin, Z.; Jimenez, I.; Gomez, M. A.; Ade, H.; Kilcoyne, A. L. D. *Macromolecules* **2010**, *43*, 448–453.
- (13) Li, Y.; Shimizu, H. *Macromol. Rapid Commun.* **2005**, *26*, 710–715.
- (14) Kontopoulou, M.; Liu, Y.; Austin, J. R.; Parent, J. S. *Polymer* **2007**, *48*, 4520–4528.
- (15) Vaia, R. A.; Giannelis, E. P. *Macromolecules* **1997**, *30*, 8000–8009.
- (16) Sung, Y. T.; Kim, Y. S.; Lee, K.; Dim, W. N.; Lee, H. S.; Sung, J. Y.; Yoon, H. G. *Polym. Eng. Sci.* **2007**, *47*, 1671–1677.
- (17) Mittal, V. J. *Appl. Polym. Sci.* **2008**, *107*, 1350–1361.
- (18) Jang, B. N.; Wang, D.; Wilkie, C. A. *Macromolecules* **2005**, *38*, 6533–6543.
- (19) Kim, D. H.; Fasulo, P. D.; Rodgers, W. R.; Paul, D. R. *Polymer* **2007**, *48*, 5308–5323.
- (20) Treece, M. A.; Zhang, W.; Moffitt, R. D.; Oberhauser, J. P. *Polym. Eng. Sci.* **2007**, *47*, 898–911.
- (21) Kawasumi, M.; Hasegawa, N.; Kato, M.; Usuki, A.; Okada, A. *Macromolecules* **1997**, *30*, 6333–6338.
- (22) Nam, P. H.; Maiti, P.; Okamoto, M.; Kotaka, T.; Hasegawa, N.; Usuki, A. *Polymer* **2001**, *42*, 9633–9640.
- (23) Lu, Q. W.; Macosko, C. W. *Polymer* **2004**, *45*, 1981–1991.
- (24) Varela, C.; Rosales, C.; Perera, R.; Matos, M.; Poirier, T.; Blunda, J.; Rojas, H. *Polym. Compos.* **2006**, *27*, 451–460.
- (25) Poncin-Epaillard, F.; Brosse, J. C.; Falher, T. *Macromolecules* **1997**, *30*, 4415–4420.
- (26) Carrino, L.; Polini, W.; Sorrentino, L. *J. Mater. Process. Technol.* **2004**, *153*, 519–525.
- (27) Masaeli, E.; Morshed, M.; Tavanai, H. *Surf. Interface Anal.* **2007**, *37*, 770–774.
- (28) Novak, I.; Borsig, E.; Hrcakova, L.; Fiedlerova, A.; Kleinova, A.; Pollak, V. *Polym. Eng. Sci.* **2007**, *47*, 1207–1212.
- (29) Martin, Z.; Gomez, M. A.; Jiménez, I. *Polymer*, submitted.
- (30) Lee, H.-S.; Fasulo, P. D.; Rodgers, W. R.; Paul, D. R. *Polymer* **2005**, *46*, 11673–11689.
- (31) Stretz, H. A.; Paul, D. R.; Li, R.; Keskkula, H.; Cassidy, P. E. *Polymer* **2005**, *46*, 2621–2637.
- (32) Stretz, H. A.; Paul, D. R. *Polymer* **2006**, *47*, 8123–8136.
- (33) Araki, T.; Ade, H.; Stubbs, J. M.; Sundberg, D. C.; Mitchell, G. E.; Kortright, J. B.; Kilcoyne, A. L. D. *Appl. Phys. Lett.* **2006**, *89*, 124106.
- (34) Si, M.; Araki, T.; Ade, H.; Kilcoyne, A. L. D.; Fisher, R.; Sokolov, J. C.; Rafailovich, M. H. *Macromolecules* **2006**, *39*, 4793–4801.
- (35) (a) Ade, H.; Hitchcock, A. P. *Polymer* **2008**, *49*, 643–675. (b) Liang, Z. M.; Yin, J.; Xu, H. J. *Polymer* **2003**, *44*, 1391–1399.
- (36) Rodriguez-Medellin, F. J.; Mata-Padilla, J. M.; Hsiao, B. S.; Waldo-Mendoza, M. A.; Vargas-Ramirez, E.; Baldes-Sanchez, S. *Polym. Eng. Sci.* **2007**, *47*, 1889–1897.
- (37) Warwick, T.; Ade, H.; Kilcoyne, D.; Kritscher, M.; Tyliczcak, T.; Fakra, S.; Hitchcock, A.; Hitchcock, P.; Padmore, H. *J. Synchrotron Radiat.* **2002**, *9*, 254–257.
- (38) Kilcoyne, A. L. D.; Tyliczcak, T.; Steele, W. F.; Fakra, S.; Hitchcock, P.; Franck, K.; Anderson, E.; Harteneck, B.; Rightor, E. G.; Mitchell, G. E.; Hitchcock, A. P.; Yang, L.; Warwick, T.; Ade, H. *J. Synchrotron Radiat.* **2003**, *10*, 125–136.
- (39) Jacobsen, C.; Wirick, S.; Flynn, G.; Zimba, C. *J. Microsc.* **2000**, *197*, 173–184.
- (40) aXis2000 is written in Interactive Data Language (IDL). It is available free for noncommercial use from <http://unicorn.mcmaster.ca/aXis2000.html>.
- (41) Fanegas, N.; Gómez, M. A.; Jiménez, I.; Marco, C.; García-Martínez, J. M.; Ellis, G. *Polym. Eng. Sci.* **2008**, *48*, 80–87.
- (42) Dhez, O.; Ade, H.; Urquhart, S. G. *J. Electron Spectrosc. Relat. Phenom.* **2003**, *128*, 85–96.
- (43) Hyuk-soo, L.; Fasulo, P. D.; Rodgers, W. R.; Paul, D. R. *Polymer* **2005**, *46*, 11673–11689.